Mapping surface defects in highly-filled wood fiber polymer composite extrusion from inline spectral analysis

Citation for the original published paper (version of record):
Pashazadehgaznagh, S., Ghanbari, R., Bek, M. et al (2023). Mapping surface defects in highly-filled wood fiber polymer composite extrusion from inline
spectral analysis. Composites Science and Technology, 242.
http://dx.doi.org/10.1016/j.compscitech.2023.110133

Composites Science and Technology 242 (2023) 110133

Contents lists available at ScienceDirect

Composites Science and Technology

journal homepage: www.elsevier.com/locate/compscitech

Mapping surface defects in highly-filled wood fiber polymer composite extrusion from inline spectral analysis

Sajjad Pashazadeh [a], Reza Ghanbari [a,b], Marko Bek [a], Alexandra Aulova [a], Tobias Moberg [c], Anders Brolin [d,e], Roland Kádár [a,e,f,*]

[a] Chalmers University of Technology, Department of Industrial and Materials Science, SE 412 96, Gothenburg, Sweden
[b] NKT Technology Consulting, SE 722 26, Västerås, Sweden
[c] Stora Enso AB, Circular Solutions, Packaging Solutions, Hylte Mill, SE 314 81, Hyltebruk, Sweden
[d] Stora Enso AB, Group Innovation and R&D, Karlstad Research Centre, SE 650 09, Karlstad, Sweden
[e] FibRe-Centre for Lignocellulose-based Thermoplastics, Department of Chemistry and Chemical Engineering, Chalmers University of Technology, SE 412 96, Gothenburg, Sweden
[f] Wallenberg Wood Science Centre, Chalmers University of Technology, SE 412 96, Gothenburg, Sweden

ARTICLE INFO

Keywords:
Melt flow instabilities
Inline spectral analysis
Wood plastic composites

ABSTRACT

Surface defects in highly-filled wood polymer composites (WPCs) are mapped in single-screw extrusion via inline optical spectral analysis for the first time. The effects of wood fiber content and drying on the dynamics of surface defects are spatio-temporally resolved via space–time inline optical imaging. Surface tearing appeared from the lowest shear rates investigated followed by a gradual decay in spectral intensity with increasing shear rates/slip velocities. This is accompanied by broadening of the surface tearing characteristic frequency while the average wavelength is estimated to remain constant within the experimental conditions. Increasing shear rates, drying and increasing wood fiber content showed mitigating effects on surface tearing. However, surface tearing in undried samples was still present even at the highest shear rates and high wall slip velocities. A regime where the extrudate surface is dominated by bubbles at high shear rates and low wood fiber contents in undried WPCs was identified.

1. Introduction

The global market for polymers with wood-based reinforcements, i.e. wood polymer composites (WPCs), was valued at $5.4 billion in 2020 and is expected to reach $12.6 billion by 2030 [1]. The annual demand for goods produced from WPCs by means of extrusion or injection molding is therefore set to increase significantly. This can be noted for several large industrial sectors of importance for the global economy such as automotive, packaging, construction, and furniture industries. In addition to the reinforcement effects, with improved stiffness and strength in WPCs, part of the plastic is replaced by a renewable material [2–5]. Therefore, WPCs are a key industrial ingredient in the context of overarching societal efforts to promote and increase the use of renewable materials [6]. A current drive for WPCs is to maximize the use of renewable content in mass production systems, with research on highly-filled compositions covering filler concentrations up to 80 wt% [6]. However, such new material formulations pose new challenges to existing processing equipment designs and raise fundamental questions about their extrusion flow dynamics. This can be the case for melt flow instabilities (MFI). The presence of MFIs in synthetic plastics is most often undesirable because they generally decrease the mechanical properties, alter the optical properties and in some cases, completely disrupt the shaping phase of plastics. However, in certain key applications, some instability modes are technology enablers and thus understanding their origin, behavior and control thereof is of utmost importance. Because of such factors, a considerable amount of research has been devoted to investigating MFI in synthetic plastics in the past several decades, with the goal of elucidating melt flow stability, create better MFI detection methods, modeling and devise means to mitigate their negative effects on processing throughput and material properties [7–18]. Overall, MFI can manifest both [15] surface irregularities, e.g. sharkskin in linear polymers [16], and surface undulations in long chain branched polymers [19–21], and volume distortions, e.g. stick–slip and gross melt fracture [7]. Their flow stability dynamics follows smooth extrudate surface (no MFI) at low control parameters, whereas above certain critical values, e.g. $\dot{\gamma}_{cr1}$ or Wi_{cr1}, the onset of MFI occurs, with a succession of modes with increasing control parameter that is particular to the molecular properties of the polymers and processing conditions.

* Corresponding author at: Chalmers University of Technology, Department of Industrial and Materials Science, SE 412 96, Gothenburg, Sweden.
E-mail address: roland.kadar@chalmers.se (R. Kádár).

https://doi.org/10.1016/j.compscitech.2023.110133
Received 26 February 2023; Received in revised form 21 June 2023; Accepted 24 June 2023
Available online 3 July 2023

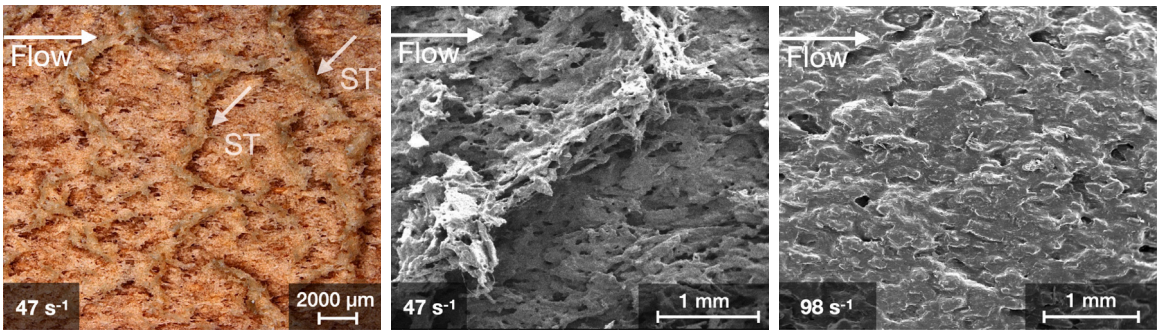

Fig. 1. Optical microscopy for undried 40 wt%, (a), scanning electron microscopy for undried 40 wt%, (b), and scanning electron microscopy for dried 40 wt%, (c); visualizations showing the presence of surface tears on the surface of a undried wood plastic composite (WPC).

In stark contrast, particularly highly-filled WPCs have proven to exhibit MFI with appearance and dynamics distinct from those encountered in neat polymers. The so-called 'surface tearing' (ST), see Fig. 1, and 'edge tearing' (ET) instabilities have been observed for the first time by Goettler et al. [22] in short fiber rubber composites. Interestingly, ST appeared at low $\dot{\gamma}$ or Wi where an increase in $\dot{\gamma}$ or Wi could lead in certain conditions to the reduction or even elimination of the instability. The effects of wood flour size and contents, matrix molecular weight, processing shear rate, and the presence of lubricants on the ST instability have been investigated by Hristov, Tákacs and Vlachopoulos in a series of publications in 2000s [23–26]. Generally, it was found that the surface of the extrudates becomes smoother with increasing shear rate, pressure and wood flour content in high density polyethylene (HDPE) wood fluor WPCs [23]. Similar behavior was also observed in HDPE composites with different wood cell wall composition such as wood flour, hemicellulose-removed particle, holocellulose, and α-cellulose by Ou et al. [27]. Further investigations revealed that increasing the wood flour content up to 50 wt% aggravated the ST, while an increase to 60 wt% wood fiber eliminated surface defects in metallocene PE (mPE)/wood flour WPCs [24]. The two observations led to a more comprehensive study where ST instabilities showed a complex dependence on shear rate, polymer matrix molecular weight, and filler particle size in mPE [25]. The addition of lubricants, coupled with increasing shear rate, was also found to mitigate surface tearing in mPE, low density polyethylene (LDPE) and an isotactic polypropylene (iPP) [26]. Interestingly, Hristov and Vlachopoulos have shown for an mPE showing stick–slip instabilities in the absence of wood flour, pressure fluctuations and non-monotonic flow curves similar to stick–slip could be induced in mPE/wood flour WPCs at high shear rates for up to 60 wt% wood flour [25]. Similar pressure fluctuations and corresponding offline optical visualizations reminiscent of the stick–slip instability have also been shown by Feng et al. (2019) in HDPE/50 wt% wood fiber WPCs [28].

To gain insight into the processing behavior of WPCs, the cited works and several other studies have focused on the rheology of WPCs [29–33]. Among the rheological parameters investigated, wall slip, as determined from capillary rheometry using the Mooney method [34], has stood out as a determinant factor in extrudate surface quality. Sufficiently high shear rates together with high wood filler contents can lead to increasing wall slip velocity thus mitigating surface tearing instabilities [23,25,26].

Mechanisms proposed for explaining ST MFI in WPCs assume a molecular slip mechanism at the walls and tensile stresses at the die exit coupled with poor polymer-filler interface causing surface tears [26], similar to the mechanisms proposed for sharkskin in neat polymers. Thus, the elimination of ST at high shear rates was attributed to very high slip velocities preventing the attachment of polymers chains to the die walls in the wall exit region. [26]. Overall, the available data in the scientific literature point to a complex behavior of MFI in WPCs with numerous influencing factors identified, however, without a systematic mapping of MFI dynamics.

In the present study, we focus on examining in detail the onset and decay of surface instabilities in highly filled wood-fiber polymer composites WPCs. In contrast to the vast majority of publications cited in this work which are focused on wood flour, we are focused on wood fiber reinforcement and compare undried and dried WPCs. In addition, we are using a single screw extruder for the inline analysis in an attempt to more realistically mimic a WPC shaping operation, in contrast to the use of a ram extruder (capillary rheometer). We apply 2D Fourier-transform analysis via space–time inline optical imaging for the first time. This level of insight in WPCs surface instability dynamics has not been previously elucidated, offering a straight-forward way to determine processing windows for WPCs. The spectral dynamics analysis is complemented by thermal characterization, capillary rheometry, including slip analysis, and oscillatory shear rotational rheometry. The results show that for dried WPCs surface tearing was detected from the onset of flow and experienced a monotonic decay in intensity accompanied by a characteristic frequency peak broadening, at approximately constant average wavelength but with diminishing tear depth, eventually reaching levels of WPC surface roughness at sufficiently high slip velocities. Generally, higher wood fiber content had a stabilizing effect on the surface properties. In contrast, undried WPCs showed two distinct transition states corresponding to 5 wt% to 10 wt% and 20 wt% to 40 wt%. Despite the lubricating potential of higher moisture contents, in both cases smooth extrudates could not be reached. For 5 wt% to 10 wt%, despite the decrease in surface tearing intensity with increasing shear rate, for shear rates above 100 1/s, a flow regime where bubbles dominate the surface appearance was detected (bubbly surface). For 20 wt% to 40 wt% the bubbly surface regime was not observed. In addition, while there was a slight decay in the intensity of the surface tearing by increasing the shear rate, the flow did not transition to a smooth extrudate flow.

2. Methods and materials

2.1. Materials

Custom compositions of Polypropylene (PP) - wood fiber WPCs based on the commercial DuraSense® WPCs produced by Stora Enso Oyj (Helsinki, Finland) were investigated in this study. A set of six wood fiber weight fractions were prepared through compounding using a co-rotating twin screw extruder (ICMA san giorgio, Italy): pure PP, 5 wt%, 10 wt%, 20 wt%, 30 wt%, and 40 wt%. The wood fibers used in the WPCs are milled fibers having a diameter of a maximum of 0.5 mm. As the moisture content of WPCs plays a crucial role in their processing and final properties, all compositions were pre-conditioned in two ways, i.e., undried and dried. Undried samples refer to WPCs with no drying (ambient conditions) before processing. Dried WPCs pellets were placed in a convection oven (Memmert Universal oven UF260plus, Germany) and were kept at 90 °C for five days prior to testing.

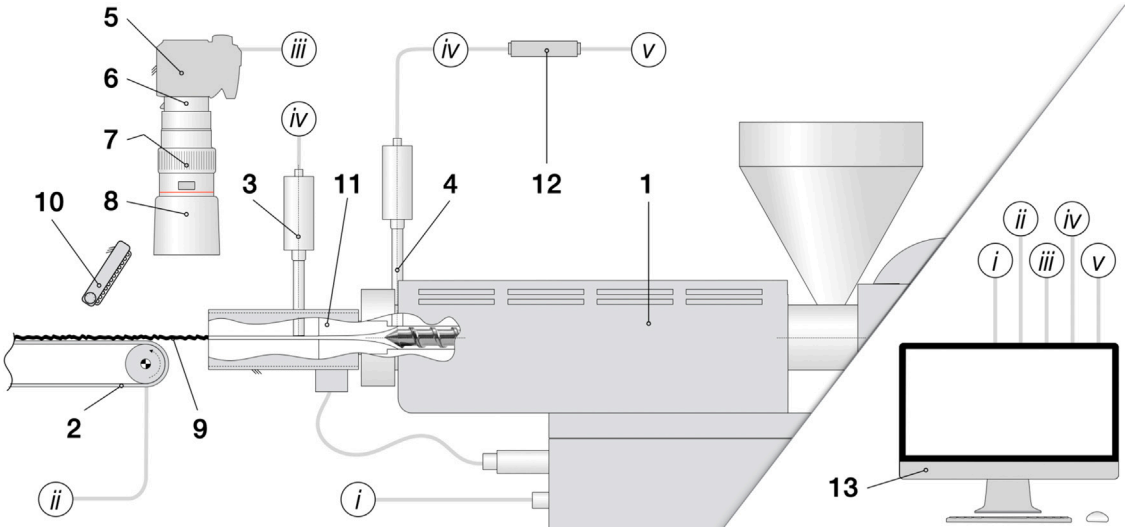

Fig. 2. Schematic of the extruder and inline optical image system: (1) single screw extruder, (2) conveyor belt, (3,4) melt pressure transducers, (5, 6, 7, 8, 9) inline optical image system (100 fps HD), (10) LED illumination system, (11) custom extrusion die, (12) data acquisition board (pressure) and (13) command and control.

2.2. Thermal characterization

Thermal characterization was performed on selected dried samples of neat PP, 5 wt% and 40 wt%. Thermal degradation was studied using thermogravimetric analysis (TGA), (Mettler Toledo, Greifensee, Switzerland). Isothermal tests at 200 °C were performed for 1.5 h in air for neat PP and 40 wt%. Temperature ramp tests were performed in a nitrogen atmosphere from 30 °C to 600 °C with the rate of 10 °C min^{-1}. Sample weight varied from 7 mg to 9 mg. Differential scanning calorimetry (DSC) was performed using a Mettler Toledo Thermal Analysis System DSC 2 (Greifensee, Switzerland). Melt and crystallization temperatures were determined based on the heat-cool-heat cycles from 25 to 220 °C in the presence of nitrogen atmosphere at the speed of heating/cooling of 10 °C min^{-1}. In order to remove the thermal history of the sample, the melting temperature and degree of crystallinity were determined from the second heating cycle. The degree of crystallinity was calculated according to the following relationship:

$$\chi = \frac{\Delta H_m}{\Delta H_{100\%}(1-\phi)}, \tag{1}$$

where ΔH_m is the sample melting enthalpy in J g^{-1} calculated as the normalized area under the thermogram, $\Delta H_{100\%} = 207$ J g^{-1} [35] is the enthalpy of an ideal 100% crystalline PP and ϕ is the amount of filler in the WPCs.

2.3. Single screw extrusion and inline optical imaging

A schematic of the extrusion setup is shown in Fig. 2. Materials were extruded using a single screw extruder (Brabender 19/25D, Germany) with a compression screw (3:1 compression ratio), and a custom viscometry slit die with channel (length × width × height) of 132 mm × 20 mm × 2 mm. The heating zones 1–4, counting from the feeding zone towards the die, were set to 150, 170, 190 and 190 °C, respectively. The screw rotational speed (n) was increased linearly from 0.1 to 150 rpm at the ramp rate of $dn/dt = 0.1$ rpm/s, which are the two limits of the instrument. Alternatively, a lengthscale normalized measure for extrusion speed is the apparent shear rate ($\dot{\gamma}_a$) inside the extrusion die, that for a slit die can be expressed as:

$$\dot{\gamma}_a = \frac{6Q_v}{WH^2}, \tag{2}$$

where W, and H are the width and height of the slit die respectively, and Q_v is the volumetric flow. For the metering zone of the screw, the volumetric flow rate is

$$Q_v = \frac{1}{2} v_z \cdot W_s \cdot H_s, \tag{3}$$

where $W_s \approx \pi Dn \tan(\varphi)\cos(\varphi)$, H_s are the width and height of the screw channel in the metering zone, φ is the screw helix angle and v_z is the flow velocity inside the channel and can be expressed as a function of the screw speed n, screw diameter D:

$$v_z = \pi \cdot D \cdot n \cdot \cos(\varphi). \tag{4}$$

Thus, considering Eqs. (2)–(4) the ramp rate expressed in apparent shear rate is $d\dot{\gamma}_a/dt = 0.11$ s^{-2}.

Pressure buildup in the extruder and loss through the die was measured by two pressure transducers, Terwin instruments, 2000 series, max 700 bar (Nottingham, UK), (3) and (4) in Fig. 2. The transducers were mounted at the extruder outlet and at a distance of 50 mm from the die exit, respectively, see Fig. 2.

2.4. Inline analysis

The extrudate was monitored inline using an optical visualization system positioned at the die exit, comprising a Canon EOS 90D DSLR camera (Tokyo, Japan) equipped with a Canon L-series 100 mm Macro lens and LED 850 lx lights (Manfrotto, Maxima ML840H), see (5)–(8) and (10) in Fig. 2. Video recordings were performed in Full HD format, i.e. 1920 × 1080 pixels, with frame rate of $f_{cam} = 100$ fps (frames per second).

Space–time visualizations were generated from the recorded videos by appending a line of pixels extracted at fixed position along the extrudate, see A-A in 3(a), from each video frame to a newly constructed image, 3(b) [18,36,37], for 2D Fourier transform analysis. The newly constructed space–time diagram has the y-axis in units of length and the x-axis to time, $dt = 1/f_{cam} = 1/100$. We note that the space–time visualizations were converted to gray-scale for image analysis.

To quantify surface properties from space–time imaging, 2D Fourier transform (2D-FFT) was applied successively on a moving window of size 500 px and an increment of 100 px (1 s). The moving window size was selected such that it would be small enough so that the extrudate velocity does not vary significantly within, but at the same time significantly larger than the time scales associated to the surface distortions investigated. Eq. (5), represents the 2D-FFT of a grayscale image (matrix) $X_{j,l}$, with $m \times n$ data points, where m, and n respectively are the number of points on the x, and y axes of a specified window frame in the space–time image, with $p, j \in [0, m-1]$ and $q, l \in [0, n-1]$.

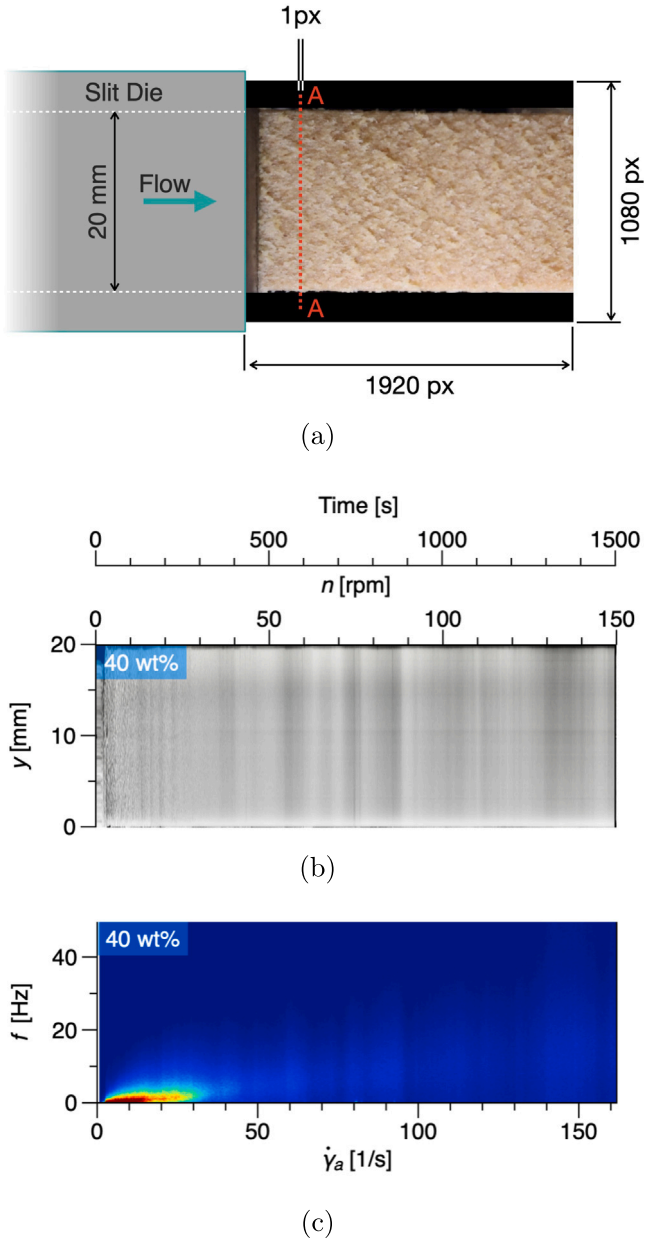

Fig. 3. (a) Schematic illustrating the visualization area and the line of pixels (A-A) extracted for the construction of space–time diagrams. (b) Example of space–time image. (c) Example of (temporal) spectrogram from 2D Fourier Transform Analysis. The examples are from tests on dried samples containing 40 wt% wood fiber.

More details regarding the Fourier transform method can be found in [38].

$$F_{p+1,q+1} = \sum_{j=0}^{m-1}\sum_{l=0}^{n-1} \kappa_m{}^{jp}\kappa_n{}^{lq} X_{j+1,l+1} \tag{5}$$

where: $\kappa_m = e^{\frac{-2\pi i}{m}}$, $\kappa_n = e^{\frac{-2\pi i}{n}}$ and $i = \sqrt{-1}$. Thus, both temporal, $F(\omega)$, and spatial, $F(k)$ characteristic frequencies of instabilities can be quantified. The temporal and spatial Fourier spectra were then collected into spectrograms to capture the time and therefore screw speed/die shear rate dependence of the characteristic surface pattern frequencies. An example comparing the space–time images and the corresponding (temporal) frequency spectrum can be found in Fig. 3(b)–(c), respectively.

The entire methodology described was implemented as a customized code in MATLAB R2020b. We note that the moving window 2D-FFT procedure can also be implemented for real-time inline quantification.

2.5. Rheological characterization

The rheological characterization of the WPCs was performed in order to have a better understanding and control over their processability. To this end, two different approaches were exploited: rotational rheometry and capillary rheometry.

2.5.1. Rotational rheometry

Oscillatory shear tests were performed on an Anton Paar MCR 702 Twin Drive rheometer (Graz, Austria) at 190 °C. PP25 serrated plates were used to minimize slip effects. Strain sweeps at a constant frequency of $\omega = 6.28$ rad/s were performed for all samples to determine the linear viscoelastic limit. Thereafter, frequency sweeps, with the angular frequency range of 0.02 to 628 rad/s, were performed at constant strain amplitude in the linear viscoelastic region, in the presence of nitrogen gas to minimize sample oxidation. For PP, 5 wt%, and 10 wt% WPCs the dynamic moduli were also measured at 175 °C to extend the frequency range using time–temperature equivalence. The obtained complex viscosity (magnitude) functions were fitted with a modified Carreau-Yasuda model through the addition of a yield stress term. [39,40]:

$$|\eta^\star|(\omega) = \frac{|\sigma_y^\star|}{\omega} + |\eta_0^\star|[1 + (\tau_{CY}\omega)^a]^{(m-1)/a}, \tag{6}$$

where $|\sigma_y^\star|$ is a yield stress estimation, ω is the angular frequency, $|\eta_0^\star|$ is the zero-shear complex viscosity magnitude, τ_{CY} is the relaxation time of the model, a is the model exponent, and m is power law index. Eq. (6) has been previously implemented by Naderi et al. [41] to describe the behavior of polypropylene nanocomposites.

2.5.2. Capillary rheometry

A Göttfert RG 20 capillary rheometer (Buchen, Germany) was used to determine the steady shear viscosity functions in the higher range of shear rates, as well as determine the slip velocity as a function of wall shear stress and shear rate. The Bagley correction was applied to correct pressure/wall shear stress values for errors due to contraction flow at the die entrance. Thus, shear stress values at each shear rate were corrected as [42]:

$$\sigma_w = \frac{\Delta P}{2(L/R + e)} \tag{7}$$

where, ΔP is the (mechanical) pressure measured inline, L is the (active) length of the capillary die, R is the radius of the capillary die, and e is the Bagley correction factor. The latter can be determined through extrapolation from a so-called Bagley plot [42], i.e., measured pressure vs. die aspect ratio (L/D). Two capillary dies with the same radius and different L/D of 20/1 and 0/1 were used.

The Weissenberg–Rabinowitsch correction, that takes the non-parabolic velocity profile of Non-Newtonian flows into account, was also applied. The true shear rate, $\dot{\gamma}$, can therefore be determined as:

$$\dot{\gamma} = \frac{3}{4}\dot{\gamma}_a + \frac{1}{4}\sigma_w \cdot \frac{d\dot{\gamma}_a}{d\sigma_w} \tag{8}$$

The Mooney method [34] was applied to determine the slip velocity as function of wall shear stress. The Mooney equation Eq. (9) for a round die is:

$$Q_v = Q_s + Q_f = \pi R^2 v_s + \frac{\pi R^3}{{\sigma_w}^3}\int_0^{\sigma_w} \dot{\gamma}_a \cdot {\sigma_{rz}}^2 d\sigma_{rz} \tag{9}$$

where Q_s and Q_f are volumetric flow rates due to slip and fluidity, respectively, v_s is the (wall) slip velocity, $\dot{\gamma}_a$ here is the apparent shear rate and is equal to $4Q_v/(\pi R^3)$, σ_{rz} is the shear stress, and σ_w is the corrected wall shear stress from Eq. (7). Eq. (9) can be simplified

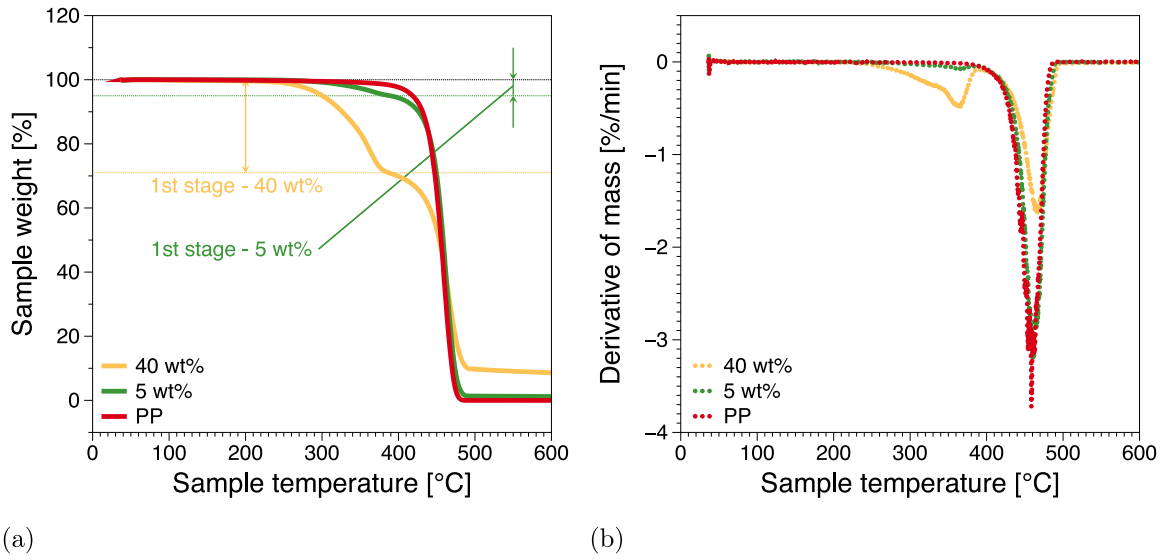

Fig. 4. TGA analysis results: (a) TGA curve — mass loss with respect to temperature, (b) DTG curve — derivative of mass loss in % with respect to temperature.

assuming a power law model [11] at higher shear rates due to the expected shear thinning behavior:

$$v_s = \frac{D}{8}\left[\dot{\gamma}_a - \frac{4n}{3n+1}\left(\frac{\sigma_w}{K}\right)^{1/n}\right], \tag{10}$$

where K and n are the consistency and flow indices. Consequently, the slip length at wall-polymer melt interface can be determined as:

$$v_s = b \cdot \dot{\gamma}_a, \tag{11}$$

where b is the slip length.

2.6. Surface profilometry

Surface profiles were measured by a KLA Tencor D-100 profilometer (Rovigo, Italy). Sample length was 2 cm and cutoff length was 5 mm.

3. Results and discussion

First, we describe the thermal and rheological behavior of the materials investigated followed by an analysis of the dynamics of surface extrudate properties as revealed by spectral dynamics based on inline optical analysis. Thereafter we validate the inline analysis with offline observations including optical microscopy, SEM and profilometry. Finally, we summarize the findings in terms of possible causes and implications for the extrusion processing of the analyzed WPCs.

3.1. Thermal characterization

Isothermal TGA tests at 200 °C in air showed that mass loss for neat PP was 9.14 % after 1.5 h exposure, while for WPC with 40 wt% of wood fibers, it was 10.22 %. During processing, material is exposed to 200 °C for a short time and it does not cause significant changes to the material. However, during rheological characterization materials were exposed to higher temperatures for prolonged time. Thus inert nitrogen atmosphere was used for rheological characterization, since isothermal tests in nitrogen atmosphere demonstrated negligible mass loss of less than 2 % (see Table 1).

TGA tests, Fig. 4 pointed to single-step and double-step mass loss for neat PP and filled materials, respectively. For the latter, the first step occurs at a temperature range of 290 to 400 °C, which corresponds to the wood fiber burning. During this step, the WPC containing 40 wt% filler lost only 28–30 % of its total mass, while for 5 wt% filler around 5 % was lost, as expected. The secondary mass loss was observed from 430 until 490 °C for all materials and can therefore be ascribed to PP degradation. Similar degradation process has been reported for analogous polymer composites [43]. The degradation of the pure polymer is completed at lower temperatures compared to the filled counterparts due to the thermal barrier effect of carbonized wood [44]. Therefore, this effect is most pronounced for the material with higher wood fiber content.

Thermal properties obtained from DSC characterization are presented in Table 2. The crystallization temperature and the degree of crystallinity were determined from the second heating cycle. There are no significant differences in melting temperature observed, as expected. However, the crystallization temperature is shifted to lower values at higher wood fiber contents, in agreement with other observations [45]. The degree of crystallinity decreases upon the addition of the wood fibers as they hinder the formation of crystalline domains of polymer chains [44]. However, the difference of crystallinity between a neat PP and the highly filled one of 40 wt% is only 2 %, which with DSC analysis, is typically considered insignificant.

3.2. Oscillatory shear

Fig. 5 presents frequency sweep (FSW) measurements for PP and WPCs. For PP, Fig. 5(a), due to the typical polymer melt behavior, the first term on the right hand side in Eq. (6) was neglected. An apparent yield stress was noticeable already at 5 wt%, Fig. 5(b). For higher concentrations (≥ 30 wt%), Fig. 5(e)–(f), only a shear thinning region could be obtained due to measurement noise at low angular frequencies.

The dynamic moduli, storage G' and loss G'', show a typical terminal region for the PP melt, 5(a), with a crossover point at $\omega = 10^3$ rad/s. Already at 5 wt%, 5(b), there is evidence of an additional elastic contribution in the limit of low angular frequencies. This, combined with the apparent yield stress in $|\eta^*|$ suggests that the sample may be at or around its percolation threshold. For WPCs with concentrations ≥ 20 wt%, a significant change in viscoelastic response can be observed with approximately equal dynamic moduli. Consequently, no characteristic relaxation time from the terminal region could be obtained.

Characteristic relaxation times are very important for estimating viscoelastic dimensionless parameters as well as for modeling. The complex viscosity profiles of pure PP and WPCs at 5, 10, and 20 wt% wood fiber contents were fitted with Eq. (6), and the fitting parameters are listed in Table 3. Characteristic (model) relaxation times, τ_{CY}, obtained from Eq. (6), as well as from cross over $1/\omega|_{G'=G''}$

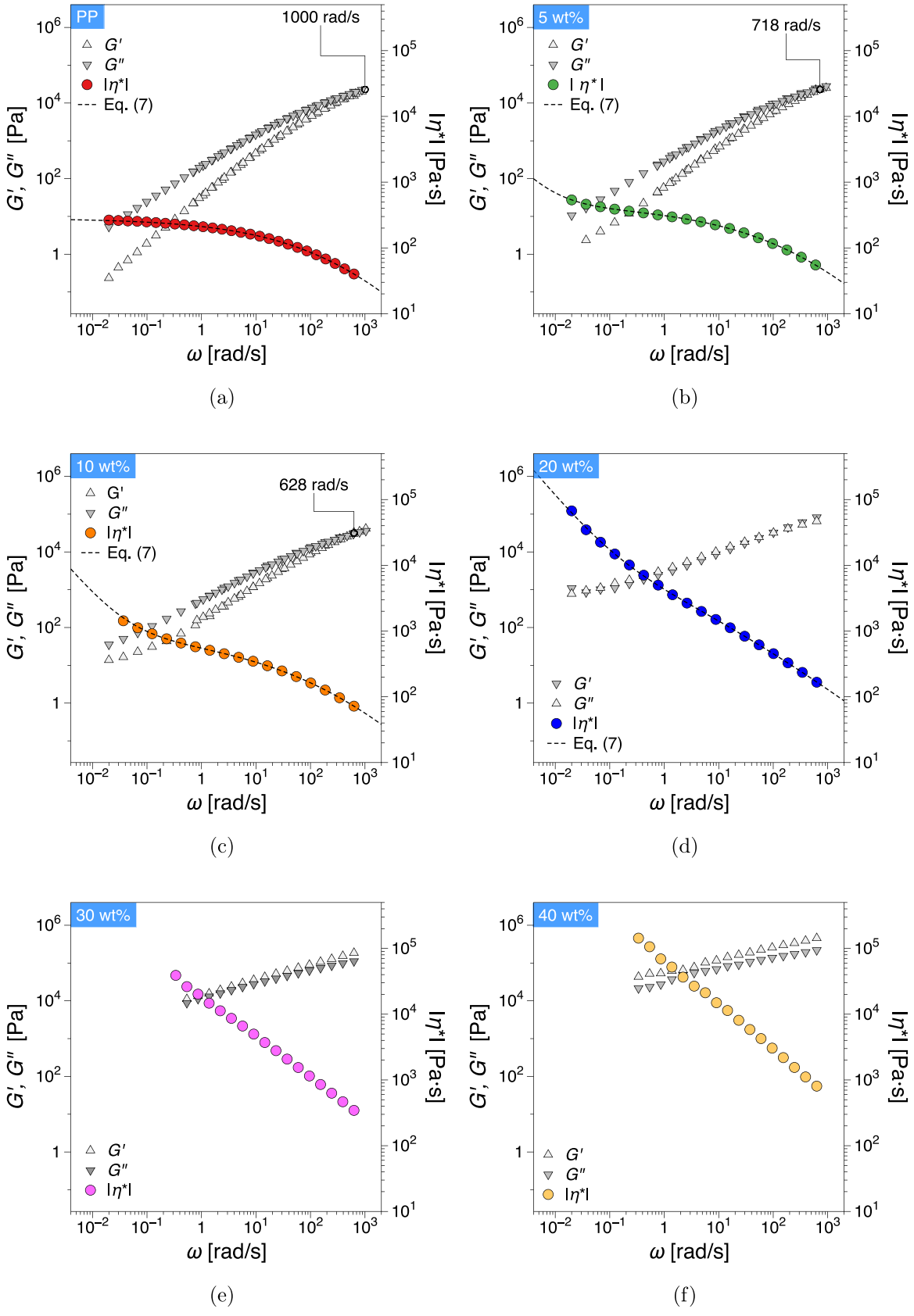

Fig. 5. Linear viscoelastic frequency sweeps tests at 190 °C: (a) PP, (b) 5 wt%, (c) 10 wt%,(d) 20 wt%, (e) 30 wt%, (f) 40 wt%. All samples tested were dried prior to the measurements.

Table 1
Summary of TGA analysis results for PP, 5 wt%, 40 wt%. T_o - onset of decomposition temperature, T_p - the peak of decomposition temperature, T_e - endpoint of decomposition temperature.

	1st stage				2nd stage			
	T_o	T_p	T_e	m_{loss}[%]	T_o	T_p	T_e	m_{loss}[%]
PP	–	–	–	–	428.09	458.82	474.52	99.84
5 wt%	305.62	369.02	409.80	5.55	435.29	460.7	474.49	92.86
40 wt%	290.74	364.11	375.19	29.71	442.24	466.06	480.95	61.57

Table 2
Thermal properties of PP, 5 wt% and 40 wt% obtained via DSC.

	T_m [°C]	T_c [°C]	ΔH_m [J/g]	χ [%]
PP	164.45	122.61	80.77	39.02
5 wt%	162.48	120.7	73.97	37.62
40 wt%	165.53	120.18	46.13	37.14

are compared in Table 3, with a good agreement found. However, no identifiable characteristic material relaxation time for concentrations above 30 wt% could be obtained directly from experimental data. This is a common issue for many similar systems. Here, we propose for the first time an arbitrary extrapolation procedure. Thus, by assuming a sigmoidal fitting, similar to the Carreau–Yasuda equation $\tau(\phi)/\tau^0_{CY} = [1+(\beta\phi)^b]^{(n-1)/b}$, the concentration dependent relaxation time, $\tau(\phi)$, can be estimated by extrapolation, see Fig. SI 2 in the supplementary information. The resulting dependence of the characteristic material relaxation time in Fig. SI 2 is similar to a percolation curve.

3.3. Capillary rheometry and slip analysis

The steady shear viscosity functions obtained from capillary rheometry are shown in Fig. 6(a), where the shear viscosity is increased at higher wood fiber content. The well-known power law model ($\eta = K\dot{\gamma}_a^{n-1}$) was used to fit the shear thinning region of the viscosity curves, and the consistency and flow indices, K and n, are listed in Table 4, a prerequisite for applying the Mooney correction Eq. (10). Fig. 6(b), (c) illustrate the slip velocity obtained from Eq. (10) as a function of the wall shear stress and apparent shear rates, respectively. According to Fig. 6(b), neat PP are prone to slip at lower wall shear stresses and have higher slip velocities compared to the filled samples as function of wall shear stress. Nevertheless, PP viscosity is lower than the WPCs, which means the wall shear stresses in PP correspond to comparatively higher apparent shear rates. Consequently, WPCs exhibit slip at slightly lower shear stresses compared to PP and exhibit higher slip velocities, Fig. 6(c). The results show that slip velocities at the highest shear rates are considerable high, reaching approximately 1/3 of the bulk (average) flow velocity. We note that for wood fiber content above 5 wt%, WPCs exhibit some degree of slip, starting with the lowest shear rates investigated. This is further highlighted by the slip length, Fig. 6(d).

3.4. Inline extrudate spectral analysis

Before discussing the space–time diagrams and their spectrograms, we make a few notes on known sources of error. At very low shear rates, see in the examples in Fig. SI 3 the region before the marked blue line, due to experimental difficulties of handling the extrudates at such low speeds, initial disturbances that are not related to instabilities are present in the spectrograms. In addition, other factors, such as fluctuations in lighting intensity and effects of moving window need to be considered at analysis. These factors can cause impersistent spectrum features (marked with purple color in Fig. SI 3(a)). By 'impersistent', we mean that for example a sudden change in lighting intensity, propagated by the moving window, can result in a baseline shift at low frequencies without any discernible or persistent peak corresponding to a surface instability. In contrast, a distinguishable peak that is persistent, see zone marked with green in Fig. SI 3(b), corresponds to the existence of extrudate surface defects.

The (mechanical) pressure variations during the stability tests can be found in Fig. SI 2. Space–time diagrams for PP, undried and dried WPCs are presented in Fig. 7 as a function of time, screw speed, and shear rate. The y-axis represents the width of the slit die while the x-axes indicate the time, screw speed, and shear rate, from top to bottom, respectively. The corresponding spectrograms, i.e. see $F(\omega)$ in Eq. (5) are displayed in Fig. 8(a), (b), and (c) for PP, dried, and undried WPCs, respectively. The y-axis represents frequency (f), in the range between 0 and 50 Hz, the Nyquist frequency of the video acquisition system. The spectrograms express the frequency spectra variation in terms of three independent variables: the apparent shear rate, $\dot{\gamma}_a$, screw speed, n, and the Weissenberg number Wi. The color map is relative for each individual test, where dark blue and dark red colors stand for low and high intensity values respectively. Based on the extrapolation procedure proposed for the characteristic relaxation time, see Fig SI. 2, the range of Wi numbers varies considerably between the PP and the WPCs with the highest wood fiber content by up to seven orders of magnitude. Corresponding spectrograms showing the spatial spectral evolution, see $F(\kappa)$ in Eq. (5), are shown in Fig. SI 4 in the supplementary information.

Based on these considerations, no instabilities are distinguishable in the corresponding spectrograms for PP, Fig. 8(a). The frequency related to the rotational speed of the screw and its corresponding harmonics can be distinguished as narrow intensity peaks that increase linearly with $n/\dot{\gamma}_a/Wi$ above $n = 70$ rpm ($\dot{\gamma}_a = 75$ 1/s, $Wi = 0.1$), Fig. 8(a). The onset of instabilities in WPCs cannot be precisely determined with space–time diagrams due to the aforementioned errors, however, from visual observations it appeared that surface tearing was present starting at the lowest shear rate investigated.

For shear rates higher than 35 1/s and in the case of dried extrudates, the intensity of the characteristic frequency associated with the ST instability starts to decay, resulting in smoother surfaces. From spectral point of view, the decay of instabilities takes place through a broadening of the characteristic frequency of the instability. This suggests that with increasing shear rate the characteristic lengthscale of the surface tears is more disperse. The onset of instabilities from low shear rates and their decay with increasing shear rates is in agreement with previous results on wood flour [23–26], suggesting that the fiber morphology may not affect the overall surface tearing dynamics. This is, again, in stark contrast to the stability of conventional polymeric materials where following an onset there is a progression of supercritical dynamic states up to gross melt fracture. We note that the decay shear rate range particularly for dried materials above 10 wt% decreases slightly to approximately 35 1/s, i.e. the addition of wood fibers has a stabilizing effect on the dynamics of surface tearing. In contrast, 5–10 wt% undried WPCs in Fig. 8(c), the spectral dynamics shows an initial decay corresponding to the intensive surface tearing at approximately 30–35 1/s, followed by an increase in intensity at 80–95 1/s. Interestingly, the initial decays are not accompanied by a noticeable broadening of the characteristic surface tearing frequency, whereas the increase in peak intensity is, suggesting it could originate from different surface phenomena, as shown further by the presence of surface bubbles. With further increase in the wood fiber content, the dynamic behavior is similar to that of dried WPCs, in that the characteristic frequency associated with surface tearing progressively decays for $\dot{\gamma}_a > 25$ 1/s, concomitantly with peak broadening. This could suggest

Table 3
Fitting parameters for the complex viscosity functions in Fig. 5 using Eq. (6).

	$\lvert\eta_0^*\rvert$ [Pa s]	$\lvert\sigma_y^*\rvert$ [Pa]	a	m	τ_{CY} [s]	τ_c [s]
PP	280.76	0	0.3452	−0.0224	0.00129	0.00099
5 wt%	438.78	2.86	0.3216	−0.00916	0.00138	0.00139
10 wt%	910.50	31.98	0.2764	−0.0369	0.00141	0.00159
20 wt%	30968.93	1063.38	0.2209	0.3230	1.4542	——

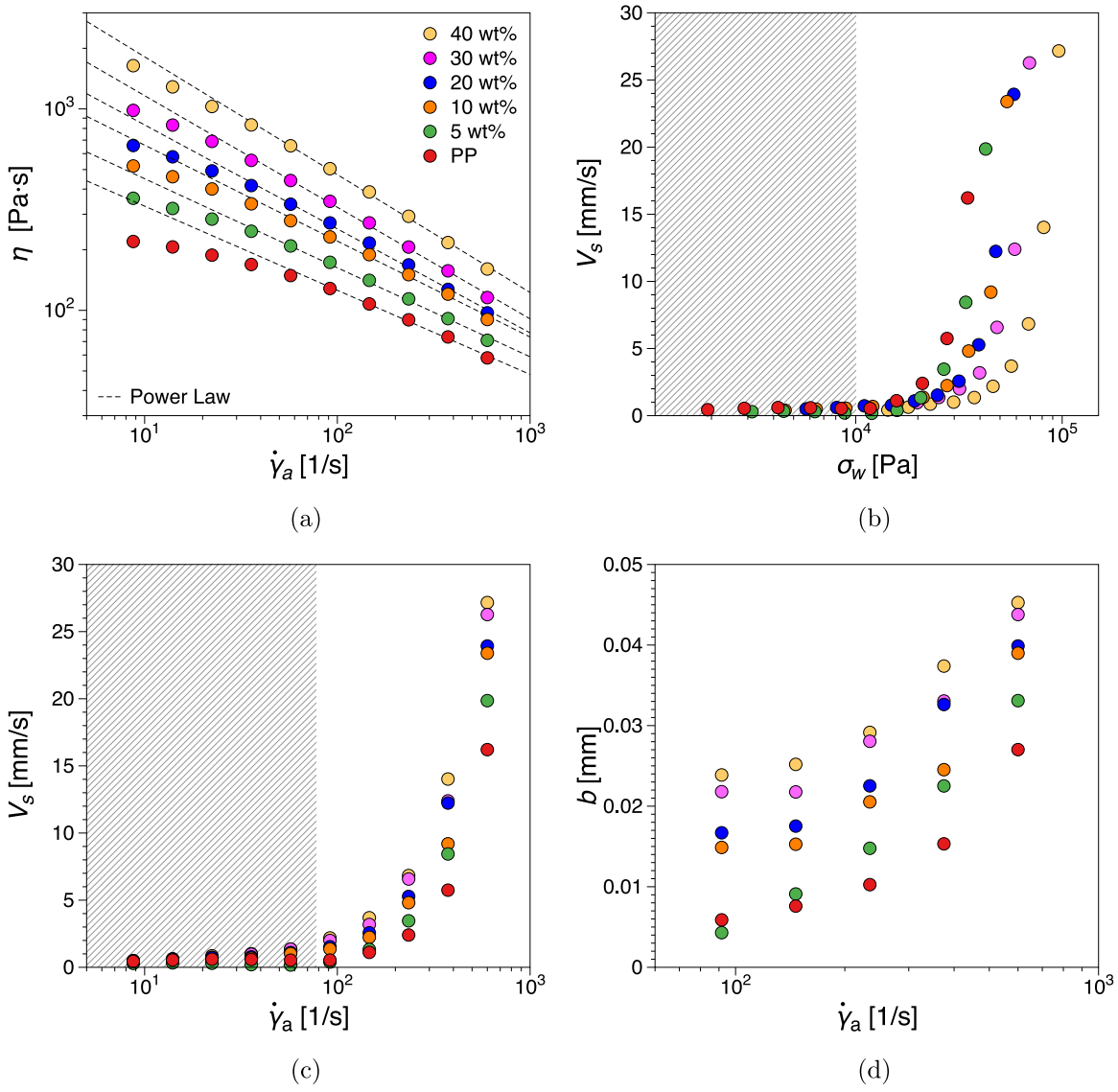

Fig. 6. Capillary rheometry results at 190 °C: (a) viscosity vs. shear rate, (b) slip velocity vs. wall shear stress (c) Slip velocity vs. shear rate, and (d) slip length vs. shear rate. The hatched regions in (b) and (c) mark datapoints where the shear viscosity deviates from the power law model.

Table 4
Fitting parameters for the viscosity functions in Fig. 6(a) using the power law model ($\eta = K\dot{\gamma}_a^{n-1}$), at $T = 190$ °C.

	PP	5 wt%	10 wt%	20 wt%	30 wt%	40 wt%
n	0.645	0.605	0.573	0.519	0.475	0.446
K	605.174	937.7851	1550.04	2300.315	3629.321	5995.855

that there could be a critical shear rate beyond which smooth surfaces could be obtained even for undried samples. Overall, the characteristic frequencies associated with surface tearing are in the range of 1-8 Hz and while for dried WPCs the scaling of the characteristic frequency with shear rate is difficult to infer, undried 20–40 wt% WPCs clearly show a linear scaling. Considering, in addition, a linear increase in extrudate velocity with increasing extrusion speed, we can infer that throughout their occurrence, surface tearing instabilities have approximately the same characteristic wavelength, i.e. $\lambda = v_e/f_{ch}$, where v_e is the extrudate velocity and f_{ch} the characteristic frequency of the surface tearing instability (maximum peak intensity). The dependence of the characteristic wavelength of surface tearing on wood fiber content is shown for undried WPCs in Fig. 9. We also note that for 5 and 10 wt% the wavelength is meant to correspond only to the ST instability. As a reference, the characteristic wavelengths obtained with slit dies of the

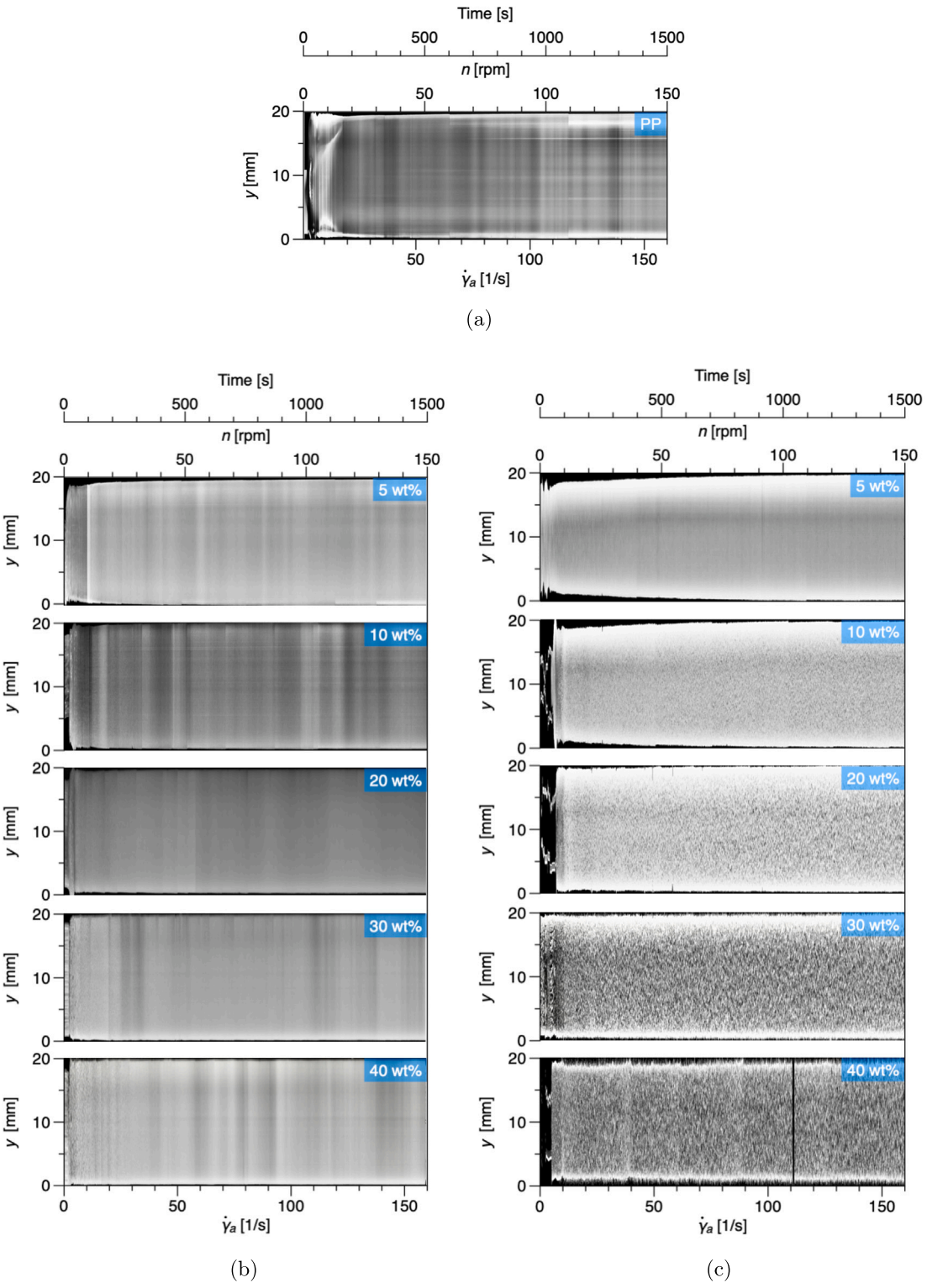

Fig. 7. Space–time optical visualizations: (a) polypropylene, (b) dried and (c) undried WPCs.

same aspect ratio, ($W/H = 10$) for the sharkskin instability and polybutadiene rubbers was found to vary from 10^{-1} mm at onset (10 1/s) up to 0.4 mm at 35 1/s [46], similar to wavelengths recorded also in linear low-density polyethylene [47] and in Styrene–butadiene rubbers. In LDPE, surface undulations corresponding to the first instability mode (not sharkskin) [19] characteristic wavelengths reached 0.7 mm. The wavelengths corresponding to the stick–slip instability are considerably higher than the ST wavelengths recorded here, however, due to the complex variation of extrudate velocity they are more difficult to estimate. We note that while the wavelength does depend on the extrusion temperature, time–temperature superposition using an Arrhenius form has been validated for sharkskin wavelengths [37]. Importantly, in

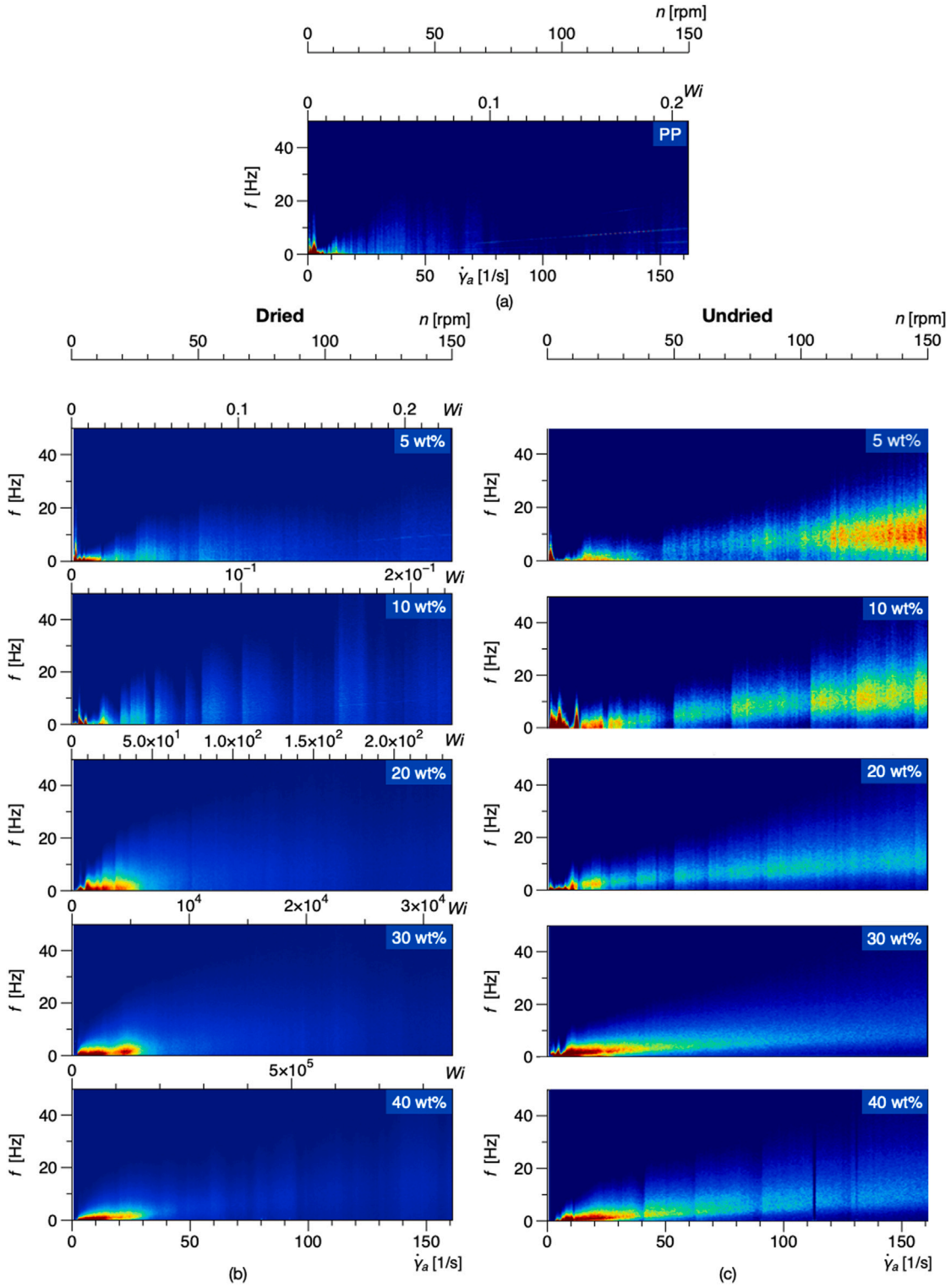

Fig. 8. Temporal spectrograms for (a) Polypropylene, (b) dried, (c) undried WPCs. Maximum and minimum contours field limits were set according to the maximum peak and maximum decay values.

all the systems cited, a power law scaling of the wavelength with increasing shear rate was found, whereas in the case of surface tearing we find that the wavelength seems to be independent of the shear rate. An important observation to make here is that the experimental design assumes quasi-steady-state conditions, most suitable for continuously mapping instabilities, whereas longer waiting times may be required to reach full steady states.

Concerning the spatial periodicity (wavenumber) of surface tearing, we briefly note that while temporal periodicities have previously been reported using other inline methods for melt flow instabilities (for example using in-situ pressure fluctuations), to our knowledge this is the first instance where the wavenumber of the instabilities is quantified for melt flow instabilities. For PP, Fig. SI 4(a), as there are no instabilities present, we can gain an estimation of the associated errors.

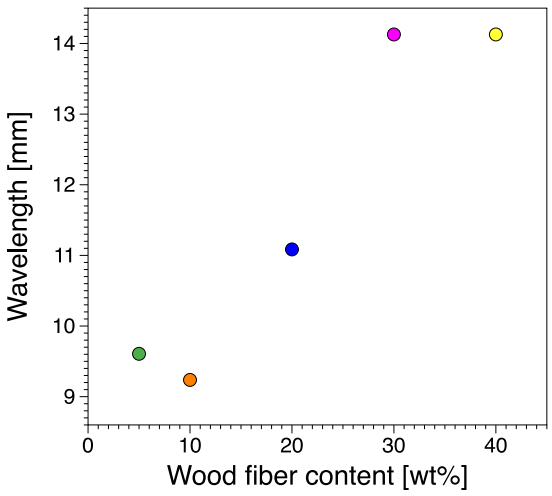

Fig. 9. Wavelength of surface instabilities as function of wood fiber content for undried WPCs.

As can be seen in Fig. 7(a) local defects likely in the construction of the die propagate as horizontal stripes that therefore are manifested in the wavenumber signal decay in the limit of low wavenunmbers. Therefore, for the dried, Fig. SI 4(b), 5, 10 wt% WPCs, we attribute the low wevenumber decay in intensity to such artifacts. However, for 20, 30, 40 wt% WPCs there appears to be a more pronounced wavenumber intensity. This loosely corresponds to the onset and decay of the characteristic surface tearing (temporal) frequency, as well as to readily observable surface patterns in the space–time diagrams. In contrast, the undried 5, 10 wt% show a distinguishable characteristic wavenumber of up to 0.1 mm^{-1} (10 wt%, highest Wi). This characteristic wavenumber appears to relate to the onset of the bubble dominated extrudate surfaces. For higher wood fiber content, the onset of a clearly distinguishable surface instability characteristic wavenumber progressively occurs at lower shear rates. However, their onset appears to correspond to a broadening and decay of the characteristic surface tearing (temporal) frequency rather than its onset. When comparing the spatial spectrograms to the space–time diagrams in Fig. 7 it can be stated that the presence of a characteristic instability wavenumber corresponds to areas where the surface patterns are well defined even in the condensed view presented in the manuscript. Thus issues of spatial resolutions may hinder the precise evaluation of spatial periodicities.

3.5. Validation of inline extrudate analysis

The Rz roughness parameter from profilometry at selected shear rates is shown in Fig. 10 and all values are listed in Table SI 1 and SI 2 in the Supplementary Information. The surface roughness measurements largely follow the surface tearing dynamics derived from spectral analysis. Dried WPCs show a gradual decay from an initial maximum, Fig. 10(a). The data further highlights the influence of wood fiber content on the surface appearance. In the 5–20 wt% range R_z values are very similar, whereas for 30 wt% the initial surface roughness is comparatively higher at low shear rates. However, it tends towards the same approximate roughness at high shear rates. For 40 wt% both at low shear rates as well as at the highest shear rates R_z is slightly higher.

In contrast, undried WPCs, Fig. 10(b), at low fiber contents ($\leq$ 10 wt%) show a noticeable increase in surface roughness above 50 1/s, a somewhat neutral dynamics at 20 wt%, while for $\geq$ 30 wt% a decrease in R_z could be observed above 100 1/s. Considering the spectral and surface roughness dynamics together provides a more complete picture of the surface tearing phenomena. Three factors can here be considered: (i) the wavelength, which is a (average) measure of the distance between two consecutive surface tears, (ii) R_z, which is a (average) measure of the depth of the tears, and (iii) broadness of the characteristic peak which is the measure of how disperse the surface tears are in time. Thus, while we have inferred a constant wavelength for surface tearing independent of shear rate, the depth of the tears decays for higher concentrations (R_z), hence the lower intensity in the characteristic ST frequency, while at the same time the distance between successive tears has a broader variability.

To address the origin of the increase in spectral intensity at higher shear rates for undried 5–10 wt%, snapshots from inline imaging as well as offline SEM images at different shear rates, space time diagram and frequency map for the undried 5 wt% WPC are represented in Fig. 11. Thus the surface tearing can be clearly evidenced starting from low shear rates. However, at very high shear rates ($\dot{\gamma}_a > 95$ 1/s), bubbles have a significant presence on the surface giving rise to elevated surface roughness.

3.6. Optimal processability windows, phenomenology and stability criteria

Spectral dynamics phase diagrams summarizing the extrudate surface states can be constructed by assuming a linear increase of the maximal (peak) characteristic frequency of the surface distortions. As the intensity of the instability has been shown to accurately represent the presence of surface defects, and depth of the ST, plotting the maximal peak intensity variation with shear rate effectively summarizes all surface states and can be used as an intuitive way to asses processing windows, see the example in Fig SI 5 in the supplementary information. Thus, flow phase diagrams for WPCs are presented in Fig. 12. We briefly note that the color mapping, relative in the present case, could also be scaled approximately to the surface roughness to have a more quantitative mapping. While handily mapping all the dynamical states achievable within the set parameter range, such diagrams could also be utilized as a highly detailed mapping of the processability windows for obtaining high-quality smooth extrudate surfaces. The dried samples of pure PP and the WPCs with 5 wt% show a very limited shear rate range of surface tearing. Interestingly, both the limit of ST in dried WPCs and the intensive ST limit in undried WPCs are shown to follow a similar trend with increasing wood fiber content, where they reach the asymptotic limit of around 30–35 1/s. This corresponds to very low slip velocities. Furthermore, for concentrations $\phi \in [5, 10]$ wt% the bubbly surface region is clearly identifiable for shear rates $\geq$ 100 1/s.

Finally, based on the analysis presented in this study, an ad-hoc empirical stability criterion of the form

$$Wi_{cr1}^{(d)} = c_0 e^{c_1 \phi} \tag{12}$$

where $Wi_{cr1}^{(d)}$ is the critical Weissenberg number associated to the decay of surface tearing and ϕ is the wood fiber content, is presented in Fig. 13. The criterion is also extrapolated to a broader range of wood fiber contents, such that in the $\phi \rightarrow 0$ limit $Wi_{cr1} \rightarrow 0$ (note the log–log representation). Technically there is no asymptotic limit before 100 wt% wood fiber, however, a limiting factor could be added as a maximum packing fraction (considering that there is also a physical limit to the relaxation time and achievable shear rates). More importantly, in the present form, the stability criterion is dominated by the magnitude of the characteristic relaxation time rather than shear rate. It is also worth noting that the experimental evidence presented does not exclude the possible existence of a Wi_{cr1} for the onset of surface tearing at very low shear rates. Although the stability criterion is very limited in its present scope and that it relies on the postulated extrapolated procedure for a characteristic material relaxation time to express the Wi, intrinsically includes three characteristic parameters, i.e. a lengthscale, velocity and a characteristic material relaxation time. Thus such criteria could be very useful for both experimental and theoretical work on the subject and could serve as a fist step to fully map the surface stability limits of highly-filled WPCs.

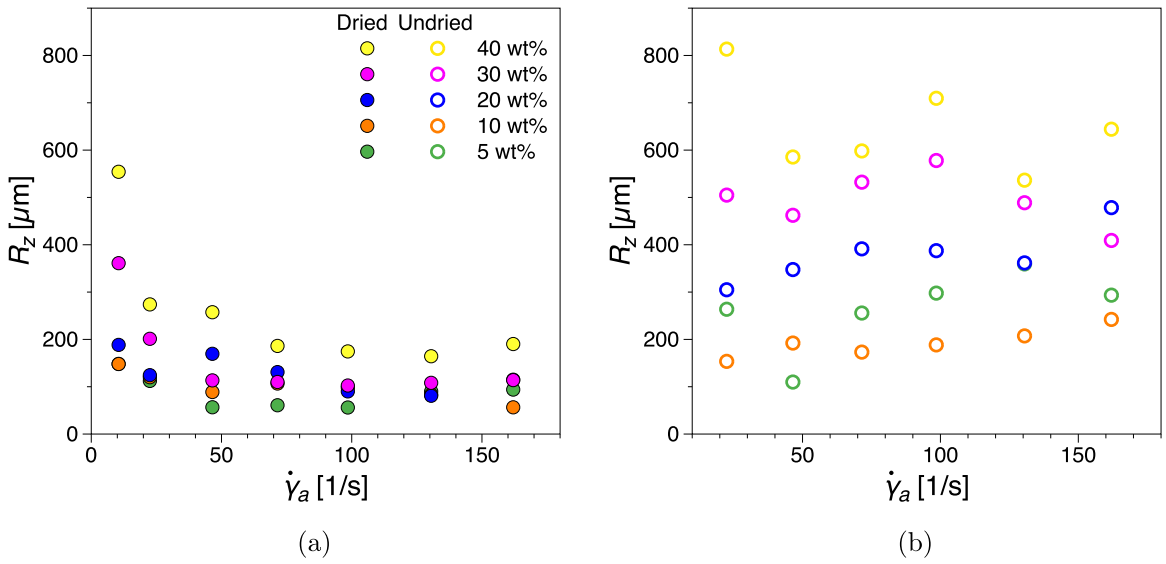

Fig. 10. *Rz* roughness parameter from profilometry at selected shear rates: (a) dried and (b) undried WPCs.

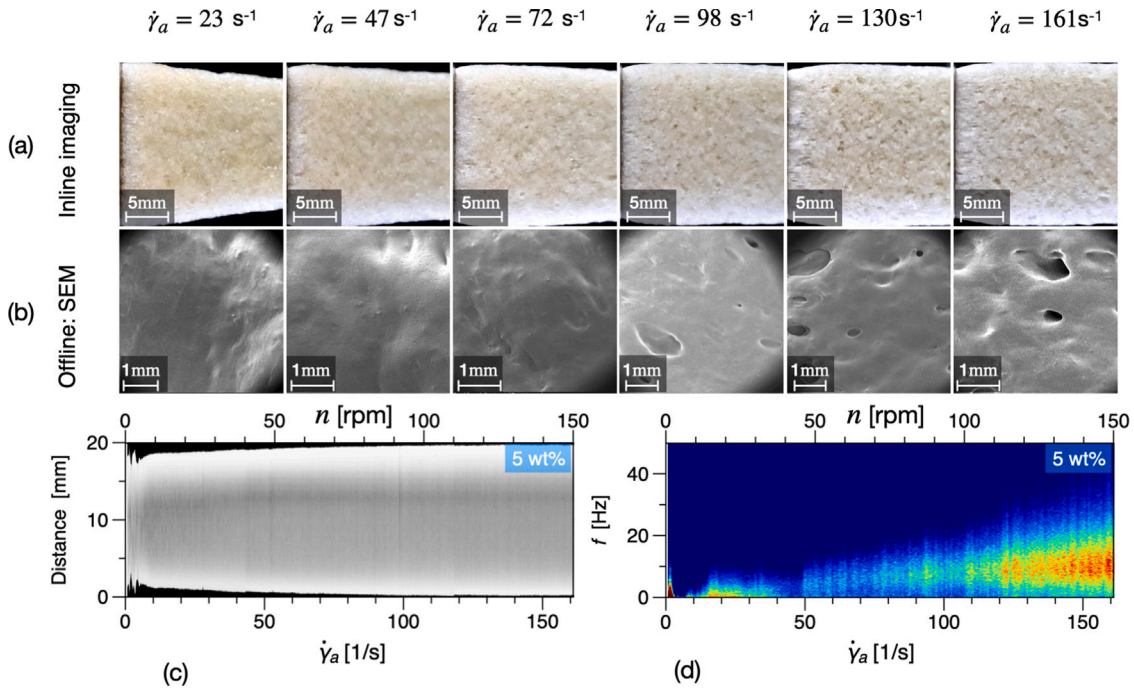

Fig. 11. Examples of optical images and SEM of to the 5 wt% WPC extrudate surface showing the presence of bubbles at the surface of the extrudates at high shear rates.

4. Summary and conclusions

We focused on the dynamics of surface instabilities during the (single-screw) extrusion of wood fiber WPCs. The WPCs investigated were polypropylene based with up to 40 wt% wood fiber content. To quantify the dynamics of surface instabilities, inline optical image analysis, comprising the acquisition of die exit video data, construction of space–time diagrams, and thereafter via 2D-Fourier transform analysis, the determination of temporal and spatial spectrograms, was performed. In addition to wood fiber content, the effect of drying was also considered. The rheological properties of WPCs were assessed using oscillatory shear and capillary rheometry. In order to address the influence of wall slip, the Mooney method was used in capillary rheometry. Thermal characterization, roughness tests and scanning electron microscopy complemented the melt flow stability analysis. Based on the spatio-temporal spectrograms, we assessed for the first time the onset and decay of surface tearing in WPCs, summarized through the construction of flow phase diagrams.

A mechanism for surface tearing has been proposed as a result of extensional rates at the die exit due to swelling and low extensional leading to surface fracture [26], similar to the sharkskin instability, but enhanced by a poor adhesion between fillers and matrix. The latter would explain why the characteristic wavelength of surface tearing is considerably larger than sharkskin. The present results, however, highlight certain aspects of MFI that may not be entirely covered by the described mechanism. Namely it is the absence of swelling that makes it difficult to trace the origin of the surface cracks in the samples investigated. Conjectures are also difficult to make in the absence of definitive proof that the mechanism for surface tearing originates at the die exit. The observed increase in the wavelength of the instabilities,

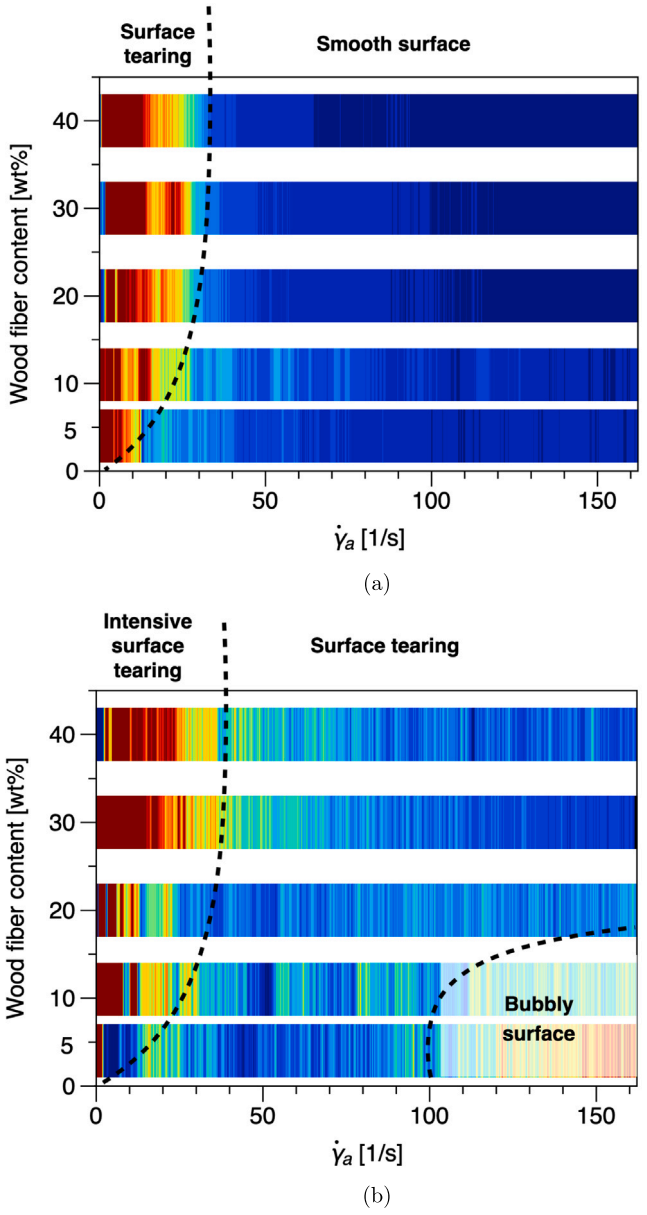

Fig. 12. Phase diagrams mapping smooth extrudates, surface tearing and the presence of bubbles: (a) dried (b) undried WPCs.

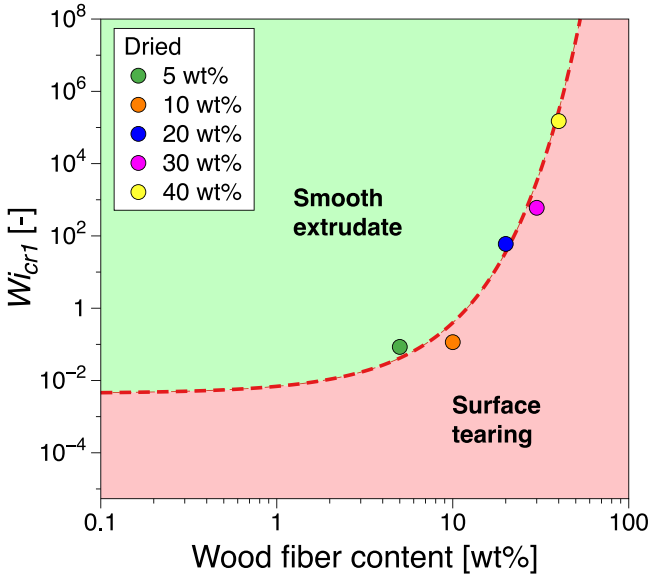

Fig. 13. Stability criterion based on the data obtained in the present study in the form of $Wi_{cr1}^{(d)}$ as the critical Weissenberg number associated with the decay of surface tearing, as a function of wood fiber content, ϕ. The criterion is extrapolated over a broader wood fiber content range.
Note: $c_0 = 0.0044, c_1 = 0.44$.

Fig. 9, could be related to the percolation threshold as can estimated from the frequency dependent behavior of the dynamic moduli, Fig. 8. What the results do confirm is that the decay in surface tearing for dried samples appears well correlated to wall slip. The presence of bubble dominated surfaces raises two questions that is why it is limited to higher shear rates and whay it only happens at wood fiber contents below 10 wt%. For higher shear rates, i.e. screw speeds, there is a decrease in the residence time inside the extruder that could lead to less efficient degassing in the transition zone. It could also be related to the very high slip velocities occurring in that shear rate range. In terms of concentration, we remark that the suppression of bubble-dominated surfaces occurs in the percolation region as well. Combining high shear rates, where towards the wall we expect a high degree of filler alignment combined with a dense network of wood fibers in the percolated core could hinder the transport of bubbles to the extrudate surface.

In addition to the stabilizing (here meaning the tendency to obtain a smooth extrudate) effect of drying and increasing wood fiber contents, a region where bubbles dominate the surface appearance of the extrudates has been identified for undried WPCs at low wood fiber contents. Two main fundamental conjectures were also proposed in the work. Firstly, we proposed a sigmoidal extrapolation of characteristic material relaxation times, a fundamental challenge for any highly filled system. Secondly, we proposed a first stability criterion for the critical Weissenberg number, $Wi_{cr1}^{(d)}$, corresponding to the decay of surface tearing in dried WPCs in the form of $Wi_{cr1} = f(\phi)$.

CRediT authorship contribution statement

Sajjad Pashazadeh: Conceptualization, Methodology, Software, Formal analysis, Investigation, Writing – original draft, Writing – review & editing, Visualization. **Reza Ghanbari:** Formal analysis, Writing – review & editing. **Marko Bek:** Formal analysis, Writing – review & editing. **Alexandra Aulova:** Formal analysis, Investigation, Writing – review & editing, Visualization. **Tobias Moberg:** Resources, Writing – review & editing, Supervision. **Anders Brolin:** Resources, Writing – review & editing, Supervision. **Roland Kádár:** Conceptualization, Methodology, Software, Writing – review & editing, Visualization, Supervision, Funding acquisition.

Declaration of competing interest

The authors declare that they have no known competing financial interests or personal relationships that could have appeared to influence the work reported in this paper.

Data availability

Data will be made available on request.

Acknowledgments

This work has been carried out within the Biocomposite program generously funded by the Knut and Alice Wallenberg foundation, Sweden (Dnr. KAW 2018.0451). Stora Enso Oyj is gratefully acknowledged for financial support.

Appendix A. Supplementary data

Supplementary material related to this article can be found online at https://doi.org/10.1016/j.compscitech.2023.110133.

References

[1] Grand View Research, Inc., Wood plastic composite market size, share & trends analysis report by type (PE, PP, PVC), by application (building & construction, automotive components, industrial and consumer goods), by region, and segment forecasts, 2022, pp. 2022–2030.

[2] L. Sobczak, R.W. Lang, A. Haider, Polypropylene composites with natural fibers and wood–general mechanical property profiles, Compos. Sci. Technol. 72 (5) (2012) 550–557.

[3] S.-Y. Leu, T.-H. Yang, S.-F. Lo, T.-H. Yang, Optimized material composition to improve the physical and mechanical properties of extruded Wood–Plastic Composites (WPCs), Constr. Build. Mater. 29 (2012) 120–127.

[4] P. Nygård, B. Tanem, T. Karlsen, P. Brachet, B. Leinsvang, Extrusion-based wood fibre–PP composites: Wood powder and pelletized wood fibres–A comparative study, Compos. Sci. Technol. 68 (15–16) (2008) 3418–3424.

[5] A. Sudár, C. Burgstaller, K. Renner, J. Móczó, B. Pukánszky, Wood fiber reinforced multicomponent, multiphase PP composites: Structure, properties, failure mechanism, Compos. Sci. Technol. 103 (2014) 106–112.

[6] M. Ramesh, L. Rajeshkumar, G. Sasikala, D. Balaji, A. Saravanakumar, V. Bhuvaneswari, R. Bhoopathi, A critical review on wood-based polymer composites: Processing, properties, and prospects, Polymers 14 (3) (2022) 589.

[7] M.M. Denn, Polymer Melt Processing: Foundations in Fluid Mechanics and Heat Transfer, Cambridge University Press, 2008.

[8] S. Hatzikiriakos, K. Migler, Polymer Processing Instabilities Control and Understanding Marcel Dekker, New York, 2005.

[9] R.G. Larson, Instabilities in viscoelastic flows, Rheol. Acta 31 (3) (1992) 213–263.

[10] T. Pakula, Nonlinear phenomena in flows of viscoelastic polymer fluids, by AI Leonov and AN Prokunin, Chapman & Hall, London 1993, 482 pp.,£ 79, ISBN 0-412-58200-7, 45, (6) Wiley Online Library, 1994, p. 436,

[11] S.G. Hatzikiriakos, Wall slip of molten polymers, Prog. Polym. Sci. 37 (4) (2012) 624–643.

[12] J. Musil, M. Zatloukal, Historical review of die drool phenomenon in plastics extrusion, Polym. Rev. 54 (1) (2014) 139–184.

[13] R. Koopmans, J. Den Doelder, J. Molenaar, Polymer Melt Fracture, CRC Press, 2010.

[14] S.-Q. Wang, Molecular transitions and dynamics at polymer/wall interfaces: Origins of flow instabilities and wall slip, in: Polymers in Confined Environments, Springer, 1999, pp. 227–275.

[15] I.F. Naue, R. Kádár, M. Wilhelm, A new high sensitivity system to detect instabilities during the extrusion of polymer melts, Macromol. Mater. Eng. 300 (11) (2015) 1141–1152.

[16] H. Palza, S. Filipe, I.F. Naue, M. Wilhelm, Correlation between polyethylene topology and melt flow instabilities by determining in-situ pressure fluctuations and applying advanced data analysis, Polymer 51 (2) (2010) 522–534.

[17] C.K. Georgantopoulos, I.F. Naue, A. Causa, L. Garro, M. Wilhelm, Investigation of melt flow instabilities in SBR: Influence of MWD and microstructure at in situ pressure fluctuations as detected by capillary rheology, Annu. Trans. Nordic Rheol. Soc 27 (2019) 151.

[18] C.K. Georgantopoulos, M.K. Esfahani, C. Botha, I.F. Naue, N. Dingenouts, A. Causa, R. Kádár, M. Wilhelm, Mechano-optical characterization of extrusion flow instabilities in styrene-butadiene rubbers: Investigating the influence of molecular properties and die geometry, Macromol. Mater. Eng. 306 (5) (2021) 2000801.

[19] R. Kádár, I.F. Naue, M. Wilhelm, First normal stress difference and in-situ spectral dynamics in a high sensitivity extrusion die for capillary rheometry via the hole effect', Polymer 104 (2016) 193–203.

[20] K.-F. Ratzsch, R. Kádár, I.F. Naue, M. Wilhelm, A combined NMR relaxometry and surface instability detection system for polymer melt extrusion, Macromol. Mater. Eng. 298 (10) (2013) 1124–1132.

[21] R. Kádár, Extrusion melt flow instabilities in long chain branched polyethylenes, Annu. Trans. Nordic Rheol. Soc. 25.

[22] L. Goettler, J. Sezna, P. DiMauro, Short fiber reinforcement of extruded rubber profiles, Rubber World 187 (HS-033 913) (1982).

[23] V. Hristov, E. Takacs, J. Vlachopoulos, Surface tearing and wall slip phenomena in extrusion of highly filled HDPE/wood flour composites, Polym. Eng. Sci. 46 (9) (2006) 1204–1214.

[24] V. Hristov, J. Vlachopoulos, A study of viscoelasticity and extrudate distortions of wood polymer composites, Rheol. Acta 46 (5) (2007) 773–783.

[25] V. Hristov, J. Vlachopoulos, Effects of polymer molecular weight and filler particle size on flow behavior of wood polymer composites, Polym. Compos. 29 (8) (2008) 831–839.

[26] V. Hristov, Melt flow instabilities of wood polymer composites, Compos. Interfaces 16 (7–9) (2009) 731–750.

[27] R. Ou, Y. Xie, M.P. Wolcott, F. Yuan, Q. Wang, Effect of wood cell wall composition on the rheological properties of wood particle/high density polyethylene composites, Compos. Sci. Technol. 93 (2014) 68–75.

[28] C. Feng, Z. Li, Z. Wang, B. Wang, Z. Wang, Optimizing torque rheometry parameters for assessing the rheological characteristics and extrusion processability of wood plastic composites, J. Thermoplast. Compos. Mater. 32 (1) (2019) 123–140.

[29] T. Li, M. Wolcott, Rheology of HDPE–wood composites. I. Steady state shear and extensional flow, Composites A 35 (3) (2004) 303–311.

[30] T. Li, M. Wolcott, Rheology of wood plastics melt. Part 1. Capillary rheometry of HDPE filled with maple, Polym. Eng. Sci. 45 (4) (2005) 549–559.

[31] T. Li, M. Wolcott, Rheology of wood plastics melt, part 2: Effects of lubricating systems in HDPE/maple composites, Polym. Eng. Sci. 46 (4) (2006) 464–473.

[32] H. Azizi, I. Ghasemi, Investigation on the dynamic melt rheological properties of polypropylene/wood flour composites, Polym. Compos. 30 (4) (2009) 429–435.

[33] M. Tazi, F. Erchiqui, F. Godard, H. Kaddami, A. Ajji, Characterization of rheological and thermophysical properties of HDPE–wood composite, J. Appl. Polym. Sci. 131 (13) (2014).

[34] M. Mooney, Explicit formulas for slip and fluidity, J. Rheology (1929-1932) 2 (2) (1931) 210–222.

[35] B.K. Wunderlich, Thermal analysis of polymeric materials, 1990.

[36] R. Kádár, I.F. Naue, M. Wilhelm, Simultaneous in-situ analysis of instabilities and first normal stress difference during polymer melt extrusion flows, Annu. Trans. Nordic Rheol. Soc. 22 (2014) 153–160.

[37] C.K. Georgantopoulos, M.K. Esfahani, C. Botha, M.A. Pollard, I.F. Naue, A. Causa, R. Kádár, M. Wilhelm, Modeling the spatial characteristics of extrusion flow instabilities for styrene-butadiene rubbers: Investigating the influence of molecular weight distribution, molecular architecture, and temperature, Phys. Fluids 33 (9) (2021) 093108.

[38] R.N. Bracewell, R.N. Bracewell, The Fourier Transform and Its Applications, Vol. 31999, McGraw-Hill, New York, 1986.

[39] F. Berzin, B. Vergnes, L. Delamare, Rheological behavior of controlled-rheology polypropylenes obtained by peroxide-promoted degradation during extrusion: Comparison between homopolymer and copolymer, J. Appl. Polym. Sci. 80 (8) (2001) 1243–1252.

[40] W. Lertwimolnun, B. Vergnes, Influence of compatibilizer and processing conditions on the dispersion of nanoclay in a polypropylene matrix, Polymer 46 (10) (2005) 3462–3471.

[41] G. Naderi, P. Lafleur, C. Dubois, Dynamically vulcanized nanocomposite thermoplastic elastomers based on EPDM/PP (Rheology & Morphology), Int. Polym. Process. 22 (3) (2007) 284–292.

[42] E. Bagley, End corrections in the capillary flow of polyethylene, J. Appl. Phys. 28 (5) (1957) 624–627.

[43] H. Jeske, A. Schirp, F. Cornelius, Development of a thermogravimetric analysis (TGA) method for quantitative analysis of wood flour and polypropylene in Wood Plastic Composites (WPC), Thermochim. Acta 543 (2012) 165–171.

[44] Y. Guo, S. Zhu, Y. Chen, D. Li, Thermal properties of wood-plastic composites with different compositions, Materials 12 (6) (2019) 881.

[45] K.P. Črešnar, L.F. Zemljič, L.S. Perše, M. Bek, Effect of wood fiber loading on the chemical and thermo-rheological properties of unrecycled and recycled wood-polymer composites, Appl. Sci. (Switzerland) 10 (2020) http://dx.doi.org/10.3390/app10248863.

[46] C.K. Georgantopoulos, M.K. Esfahani, M.A. Pollard, I.F. Naue, A. Causa, R. Kádár, M. Wilhelm, Derivation of a qualitative model for the spatial characteristic wavelength of extrusion flow instabilities: Investigation of a polybutadiene rubber through capillary, slit and complex geometry extrusion dies, Macromol. Mater. Eng. 2200313.

[47] C. Georgantopoulos, M. Esfahani, I.F. Naue, A. Causa, M. Wilhelm, R. Kádár, Investigating the role of molecular architecture and temperature on extrusion melt flow instabilities of industrial polyethylenes via capillary rheology, high-pressure-sensitivity-slit die and optical analysis, J. Appl. Polym. Sci. (2022) e53165.